WIND ENERGY
Wind Energ. 2015; **00**:1–14
DOI: 10.1002/we

arXiv:1511.04117v2 [physics.flu-dyn] 10 May 2016

RESEARCH ARTICLE

Optimal smoothing length scale for actuator line models of wind turbine blades

L.A. Martínez-Tossas[1], M.J. Churchfield[2], and C. Meneveau[1]

[1]Department of Mechanical Engineering, Johns Hopkins University, Baltimore, MD 21218, USA
[2]National Renewable Energy Laboratory, Golden, CO

ABSTRACT

The actuator line model (ALM) is a commonly used method to represent lifting surfaces such as wind turbine blades within Large-Eddy Simulations (LES). In the ALM the lift and drag forces are replaced by an imposed body force which is typically smoothed over several grid points using a Gaussian kernel with some prescribed smoothing width ϵ. To date, the choice of ϵ has most often been based on numerical considerations related to the grid spacing used in LES. However, especially for finely resolved LES with grid spacings on the order of or smaller than the chord-length of the blade, the best choice of ϵ is not known. In this work, a theoretical approach is followed to determine the most suitable value of ϵ. Firstly, we develop an analytical solution to the linearized flow response to a Gaussian lift and drag force and use the results to establish a relationship between the local and far-field velocity required to specify lift and drag forces. Then, focusing first on the lift force, we find ϵ and the force center location that minimize the square difference between the velocity fields induced by the Gaussian force and 2D potential flow over Joukowski airfoils. We find that the optimal smoothing width ϵ^{opt} is on the order of 14-25% of the chord length of the blade, and the center of force is located at about 13-26% downstream of the leading edge of the blade, for the cases considered. These optimal values do not depend on angle of attack and depend only weakly on the type of lifting surface. To represent the drag force, the optimal width of the circular Gaussian drag force field is shown to be equal to the momentum thickness of the wake. It is then shown that an even more realistic velocity field can be induced by a 2D elliptical Gaussian lift force kernel, and the corresponding optimal semi-axes ϵ_x and ϵ_y lengths are determined using the velocity matching method. Copyright © 2015 John Wiley & Sons, Ltd.

KEYWORDS

Actuator Line Model; Large Eddy Simulations

Correspondence

Journals Production Department, John Wiley & Sons, Ltd, The Atrium, Southern Gate, Chichester, West Sussex, PO19 8SQ, UK.

Received . . .

1. INTRODUCTION

Numerical simulations of flow over wind turbines often cannot afford to resolve the entire rotating blade geometry and the associated flow details [1]. Actuator disk models (ADM) greatly reduce resolution requirements by replacing the rotor by a distributed body force at the rotor disk location [2, 3]. However, the ADM misses important information about the instantaneous blade location and rotation, its detailed aerodynamic properties, etc. An intermediate approach is provided by the actuator line model (ALM) [4], a technique for simulating lifting surfaces within flow simulations with characteristics that fall in between full blade resolution and the ADM. The ALM has been particularly popular in large-eddy simulations (LES) of wind turbine blades [4, 5, 6, 7, 8, 9, 10, 11, 12]. At any blade cross-section, the local lift and drag forces,

†Please ensure that you use the most up to date class file, available from the WE Home Page at
http://www3.interscience.wiley.com/journal/6276/home

Copyright © 2015 John Wiley & Sons, Ltd.

Prepared using weauth.cls [Version: 2010/06/17 v1.00]

which are evaluated locally using tabulated lift and drag coefficients as function of the local angle of attack, are imposed at points moving with the blades within the simulation domain. The actuator surface model (ASM) is another method to represent lifting surfaces [13, 14]. In the ASM the blades are represented as a infinitesimal sheet with a vorticity source. Previous work has shown improvements in the flow fields produced by the ASM compared to the ALM [13]. The present work focuses on the ALM because of its simplicity, and its wide and common usage in representing wind turbine blades in Large Eddy Simulations [4].

In the ALM, it is common practice to smooth the imposed force using a Gaussian kernel to distribute the imposed point force. The 3D kernel is given by

$$\eta_\epsilon = \frac{1}{\epsilon^3 \pi^{3/2}} e^{-r^2/\epsilon^2}. \tag{1}$$

Here r is the distance to the actuator point and ϵ establishes the kernel width. This function is introduced to prevent numerical issues that can arise from the application of discrete body forces in a computational domain [4]. Other studies have addressed various aspects of this kernel [6]. Specifically, the effects of the parameter ϵ on ALM predictions of power and wake structures in wind turbines have been examined in previous work [10, 11], where it was also hypothesized that ϵ should physically scale with the chord length of the blade, absent numerical constraints. Although there are a number of guidelines on how to choose ϵ depending mostly on the numerics and grid resolution, no clear physical rationale for choosing a particular value of ϵ has been proposed to date.

In this work, we present a calculation of the optimal value of the Gaussian width ϵ, and of the best location to center the force, based on physical arguments instead of relying only on numerical justifications. The optimal values we seek will be based on the ability of the ALM to reproduce the induced velocity distributions as realistically as possible. An extension is presented for a 2D Gaussian kernel with different smoothing lengths in the chord and thickness directions of the airfoil.

2. FORMULATION

We develop an analytical solution to the 2D flow generated when using the ALM with a smoothing length-scale ϵ. Specifically, we consider the Euler equations in which a lift force (with circulation Γ) has been applied in the y-direction perpendicular to the free-stream velocity $U_\infty \hat{\boldsymbol{i}}$ in the x-direction. We consider the flow in the frame of reference moving with the blade cross-section, so that in turbomachinery applications the far-field velocity $U_\infty \hat{\boldsymbol{i}}$ includes the rotor tangential velocity and axial induction. In this frame, the corresponding solutions are denoted as the velocity and pressure fields $\mathbf{u}_\epsilon(x,y) = [u_\epsilon(x,y), v_\epsilon(x,y)]$ and $p_\epsilon(x,y)$ respectively. They are solutions to:

$$\mathbf{u}_\epsilon \cdot \nabla \mathbf{u}_\epsilon = -\nabla p_\epsilon/\rho - \hat{\boldsymbol{j}} \, \frac{U_\infty \Gamma}{\epsilon^2 \pi} \, e^{-(\mathbf{x}-\mathbf{x}_0)^2/\epsilon^2}, \qquad \nabla \cdot \mathbf{u}_\epsilon = 0, \tag{2}$$

subject to boundary condition $\mathbf{u}_\epsilon = U_\infty \hat{\boldsymbol{i}}$ as $|\mathbf{x}| \to \infty$. Note that we are considering the flow in 2D sections and thus neglect 3D end effects. We are also neglecting Coriolis accelerations, and viscous and turbulence effects. An analytical solution to the linearized problem, valid for small lift forces, will be derived in §3, as a function of ϵ. To establish the best value of ϵ, we seek to compare the obtained solution to the model problem with an "exact" solution of 2D flow past a lifting surface. As ground truth we use the potential flow solution to the Euler equations with the appropriate boundary conditions on the blade and the separation point at the trailing edge. We denote the potential flow solution as the velocity and pressure fields, $\mathbf{u}_p(x,y) = [u_p(x,y), v_p(x,y)]$ and $p_p(x,y)$ respectively. These fields solve the Euler equations without the force, but with the appropriate boundary conditions at the blade surface:

$$\mathbf{u}_p \cdot \nabla \mathbf{u}_p = -\nabla p_p/\rho, \qquad \nabla \cdot \mathbf{u}_p = 0, \quad \mathbf{u}_p \cdot \mathbf{n} = 0 \ \text{ on blade surface}, \tag{3}$$

and, again, the boundary condition at infinity is $\mathbf{u}_p = U_\infty \hat{\boldsymbol{i}}$ as $|\mathbf{x}| \to \infty$. The vector $\mathbf{n}$ is the unit vector normal to the blade surface. Also, the Kutta condition is implied with the separation point positioned at the trailing edge. For convenience, we use Joukowski airfoils and use the corresponding analytical solutions, recalled succinctly in §4.

Our goal is to determine the values of ϵ and $\mathbf{x}_0$ for which the difference $\mathbf{u}_\epsilon(x,y) - \mathbf{u}_p(x,y)$ between the two velocity fields is minimized, in some sense. The precise definition of the associated error norm, its minimization, and results are described in §5. It is important to recall that while the ideal velocity field is potential flow, the velocity field arising from Euler equation with a Gaussian body force is not potential since the body

Wind Energ. 2015; **00**:1–14 © 2015 John Wiley & Sons, Ltd.
DOI: 10.1002/we
Prepared using weauth.cls

force is rotational. Still, we expect that the position $\mathbf{x}_0$ and scale ϵ of the force can be chosen so as to best approximate the potential flow velocity field over a realistic lifting surface.

Furthermore, we consider the case of a drag force, in which a force in the $\hat{\boldsymbol{i}}$ direction is applied with a Gaussian distribution of width ϵ_d. In §3.2 we use the analytical solution to the linearized problem to determine a correction to the local velocity to infer the far-field velocity. We discuss the possibility of applying the drag force using a kernel width ϵ_d that could differ from that for the lift force.

3. LINEARIZED EULER EQUATION WITH GAUSSIAN BODY FORCES

Here, an analytical solution to Eq. 2 is sought. The equations are linearized about the free-stream velocity, where the velocity perturbation $u' << U_\infty$. A similar equation with a drag force instead of a lift force is used to understand the effects of a local streamwise body force on the flow. The analytical solutions are used to relate the local velocity sampled at the center of the Gaussian lift and drag force distributions with the far-field velocity needed in applications of the ALM. Then the solutions can be used to determine optimal kernel width.

3.1. Solution with Lift Force

We begin by non-dimensionalizing the problem using U_∞ as velocity scale, and the lifting surface's chord length c as length scale. We denote non-dimensional variables using asterisks, i.e $x_* = x/c$, $y_* = y/c$, $\epsilon_* = \epsilon/c$, $u_* = u/U_\infty$, $v_* = v/U_\infty$, and dimensionless circulations $\Gamma_* = \Gamma/cU_\infty$ and $K_* = \Gamma_*/2\pi$. In order to eliminate pressure from equation 2 we take its curl and obtain an equation for the scalar dimensionless vorticity $\omega_{\epsilon*}$ in the z-direction:

$$\mathbf{u}_{\epsilon*} \cdot \nabla \omega_{\epsilon*} = -[\nabla \times \frac{2K_*}{\epsilon_*^2} e^{-(x_*^2+y_*^2)/\epsilon_*^2} \hat{\boldsymbol{j}}\,]_z. \tag{4}$$

In expanded form, the equation reads

$$u_{\epsilon*}\frac{\partial \omega_{\epsilon*}}{\partial x_*} + v_{\epsilon*}\frac{\partial \omega_{\epsilon*}}{\partial y_*} = 4x_*\frac{K_*}{\epsilon_*^4} e^{-(x_*^2+y_*^2)/\epsilon_*^2}. \tag{5}$$

We now consider the small K_* behavior, and use a linear perturbation analysis around $K_* = 0$. The baseline solution is uniform flow in the x-direction and zero vorticity, i.e. $\mathbf{u}_{\epsilon*} = \hat{\boldsymbol{i}} + \mathbf{u}'_{\epsilon*}$ and $\omega_{\epsilon*} = \omega'_{\epsilon*}$ so that

$$\mathbf{u}_{\epsilon*} \cdot \nabla \omega_{\epsilon*} \approx \frac{\partial \omega'_{\epsilon*}}{\partial x_*} = 4x_*\frac{K_*}{\epsilon_*^4} e^{-(x_*^2+y_*^2)/\epsilon_*^2}. \tag{6}$$

Following Ref. [15] (their Appendix) we integrate in x_*, and using the condition that the perturbation vorticity vanishes at infinity leads to

$$\omega'_{\epsilon*}(x_*, y_*) = -\frac{2K_*}{\epsilon_*^2} e^{-(x_*^2+y_*^2)/\epsilon_*^2}. \tag{7}$$

As shown in [15] for more general cases, the vorticity distribution is proportional to the local body force. This occurs because the source of vorticity is the curl of the body force, which when integrated along the streamlines yields a distribution proportional to the body force.

The next step is to obtain the induced velocity from the vorticity distribution. The velocity field induced by a circular Gaussian vorticity distribution is a standard solution that can be obtained in polar coordinates, where the circulation around a circle of radius r_* centered at the force center is given by

$$2\pi\ r_*\ V'_{\theta,\epsilon*}(r_*) = \int\int \omega'_{\epsilon*} dA_* = 2\pi \int_0^{r_{*\epsilon}} \frac{2K_*}{\epsilon_*^2} e^{-r'^2_*/\epsilon^2}\ r'_* dr'_*. \tag{8}$$

Here $V'_{\theta,\epsilon*}$ is the tangential component of the vorticity-induced perturbation velocity:

$$V'_{\theta,\epsilon*}(r_*) = K_*\ \frac{1}{r_*}\ \left(1 - e^{-r_*^2/\epsilon_*^2}\right). \tag{9}$$

The complete solution is the perturbation added to the base flow, which when expressed in Cartesian coordinates with the Gaussian kernel centered at $\mathbf{x}_{0*} = (x_{0*}, y_{0*})$ reads

$$u_{\epsilon*} = 1 + K_*\frac{y_* - y_{0*}}{(x_* - x_{0*})^2 + (y_* - y_{0*})^2}\left[1 - e^{-\left((x_*-x_{0*})^2+(y_*-y_{0*})^2\right)/\epsilon_*^2}\right] \tag{10}$$

$$v_{\epsilon*} = -K_*\frac{x_* - x_{0*}}{(x_* - x_{0*})^2 + (y_* - y_{0*})^2}\left[1 - e^{-\left((x_*-x_{0*})^2+(y_*-y_{0*})^2\right)/\epsilon_*^2}\right] \tag{11}$$

3.2. Solution with Drag Force

Often in applications of ALM, the distributed force also includes a drag component acting (in our coordinate system) in the $x-$direction. Let us consider the problem separately from the lift force, and consider the linearized problem when we apply a drag force F_D (in 2D per unit length) using the ALM with a Gaussian kernel of width ϵ_d (the subscript stands for "drag"). The linearized evolution equation for the perturbation vorticity due to the imposed drag force now reads:

$$U_\infty \hat{\boldsymbol{i}} \cdot \nabla \omega'_{\epsilon d} = -\left[\nabla \times \left(\frac{F_D}{\rho \epsilon_d^2 \pi} e^{-(x^2+y^2)/\epsilon_d^2} \, \hat{\boldsymbol{i}} \right) \right]_z . \tag{12}$$

Normalizing and expanding yields

$$\frac{\partial \omega'_{\epsilon_d *}}{\partial x_*} = -\frac{c_d}{\epsilon_{d*}^4 \pi} \, y_* \, e^{-(x_*^2+y_*^2)/\epsilon_{d*}^2}, \tag{13}$$

where $c_d = F_D/(\frac{1}{2}\rho U_\infty^2 c)$ is the drag coefficient. Integration in x between $-\infty$ to x_* leads to a vorticity distribution given by

$$\omega'_{\epsilon_d *}(x_*, y_*) = -\frac{c_d}{2\sqrt{\pi}\, \epsilon_{d*}^3} \, y_* \, e^{-y_*^2/\epsilon_{d*}^2} \left[1 + \mathrm{erf}(x_*/\epsilon_{d*})\right]. \tag{14}$$

The x-direction velocity in the far-field (at $x_* >> 1$ where the vertical velocity $v_{\epsilon *}$ is negligible) can be obtained by integrating $\partial u_{\epsilon_d *}/\partial y_* = -\omega'_{\epsilon_d *}$, leading to the defect perturbation velocity distribution

$$u'_{\epsilon_d *}(x_*, y_*) = -\frac{c_d}{2\epsilon_{d*}\sqrt{\pi}} \, e^{-y_*^2/\epsilon_{d*}^2} \qquad \text{for} \quad x_* >> 1. \tag{15}$$

The 'initial' wake profile imposed by the Gaussian body force in the ALM in the spanwise y_* direction is therefore a Gaussian of width ϵ_{d*}. Its deficit magnitude grows initially in the x-direction within the kernel region.

3.3. Velocity Sampling in ALM

In ALM one commonly samples the velocity at the center of the applied Gaussian force and uses this velocity instead of U_∞ to determine forces based on given lift and drag coefficients [10]. This is usually done in the center of the Gaussian kernel [4, 6, 10], but others have tried different approaches [15]. Here we use the analytical solutions obtained above to clarify where the velocity may be sampled and how to correct the sampled velocity. We consider the effects of lift and drag separately.

In terms of lift, we immediately note from the analytical solution (Eq. 10) that $\mathbf{u}_{\epsilon *}(x_0, y_0) = U_\infty \hat{\boldsymbol{i}}$, i.e. at the center point of the imposed force (also the vortex center) the perturbation velocity vanishes. Thus the resulting velocity there equals the free-stream velocity, even in the presence of an imposed ALM lift force. Therefore, sampling the velocity at the center of the Gaussian applied lift force provides the free stream velocity automatically thus justifying the more common approach to sample velocities in ALM applications (see [15]) for more general treatments).

In the presence of drag, however, the situation is different as the velocity at the force center is affected by the imposed force. In order to quantify this effect, we must find the perturbation velocity at the center of the Gaussian drag force that results from the perturbation vorticity distribution in Eq. 14. To this effect we use the 2D Biot-Savart equation evaluated at the origin (center of Gaussian):

$$u'_{\epsilon_d *}(0,0) = \frac{1}{2\pi} \int_{-\infty}^{\infty} \int_{-\infty}^{\infty} \frac{y_* \, \omega'_{\epsilon_d *}(x_*, y_*)}{(x_*^2 + y_*^2)} \, dx_* \, dy_* \tag{16}$$

A change of variables is used to express x and y in terms of ϵ_d by $x_{*\epsilon} = x_*/\epsilon_{d*}$. Replacing the vorticity distribution of Eq. 14, the perturbation velocity at the origin can then be expressed according to

$$\frac{u'_{\epsilon_d *}(0,0)\, \epsilon_{d*}}{c_d} = -\frac{1}{4\pi^{3/2}} \int_{-\infty}^{\infty} \int_{-\infty}^{\infty} \frac{y_{*\epsilon}^2}{(x_{*\epsilon}^2 + y_{*\epsilon}^2)} \, e^{-y_{*\epsilon}^2} \left[1 + \mathrm{erf}(x_{*\epsilon})\right] dx_{*\epsilon} \, dy_{*\epsilon} \tag{17}$$

By anti-symmetry of the error function, the $x_{*\epsilon}$ integration only contains the $1/(x_{\epsilon *}^2 + y_{\epsilon *}^2)$ term and thus

$$-\frac{u'_{\epsilon_d *}\, \epsilon_{d*}}{c_d} = \frac{1}{4\sqrt{\pi}} \int_{-\infty}^{\infty} |y_{*\epsilon}| \, e^{-y_{*\epsilon}^2} dy_{*\epsilon} = \frac{1}{4\sqrt{\pi}} \approx 0.141 \tag{18}$$

Wind Energ. 2015; **00**:1–14 © 2015 John Wiley & Sons, Ltd.
DOI: 10.1002/we
Prepared using weauth.cls

From Eq. 18 the following observation can be made. The streamwise velocity at the center due to a drag body force is given by

$$u_{\epsilon_d}(x_0, y_0) = U_\infty + u'_{\epsilon_d}(x_0, y_0) = U_\infty \left(1 - \frac{1}{4\sqrt{\pi}}\, c_d\, \frac{c}{\epsilon_d}\right). \tag{19}$$

Therefore, based on $u_{\epsilon_d}(x_0, y_0)$, the velocity sampled at the center of the Gaussian, the free stream reference velocity may be estimated according to

$$U_\infty = \frac{u_{\epsilon_d}(x_0, y_0)}{1 - \frac{1}{4\sqrt{\pi}}\, c_d\, \frac{c}{\epsilon_d}}, \tag{20}$$

which can then be used in the determination of lift and drag forces.

The degree of nonlinearity is given by the ratio u'/U_∞, i.e. $\frac{1}{4\sqrt{\pi}}\, c_d\, \frac{c}{\epsilon_d}$. For $c_d < 1$, even choosing $\epsilon_d \sim c$ we see that the nonlinearity is less that 0.14. We have simulated a Gaussian force in a fully nonlinear 2D Navier-Stokes solver (not shown) and verified empirically that the correction factor in Eq. 20 is accurate at least up to $\frac{1}{4\sqrt{\pi}}\, c_d\, \frac{c}{\epsilon_d} \approx 0.28$ so that we believe the correction in Equation 20 can be applied quite broadly in practice.

4. POTENTIAL FLOW OVER JOUKOWSKI AIRFOIL

Next, we briefly review potential flow solution for flow over a Joukowski airfoil to be used as "ground truth" to compare the velocity field induced by a Gaussian lift force distribution. Potential flow over a Joukowski airfoil is found by mapping the solution of flow over a lifting cylinder onto the new complex space. It involves the complex velocity $w(\zeta)$ where ζ is the complex position variable $\zeta = \chi + i\psi$. Again U_∞ is the far-field velocity, and now R is the cylinder radius, α is the angle of attack, μ is a shift in the complex plane, and $\Gamma = 2\pi K$ is the circulation. Symmetric and cambered airfoils can be generated by shifting the solution in the complex plane by μ. Again the equations are made non-dimensional using the chord length for the resulting airfoil c: $\zeta_* = \zeta/c$, and the dimensionless circulation $K_* = K/U_\infty c$ is the same as that implied by the Gaussian body force considered in the prior section. The complex velocity [16] can now be written in non-dimensional form according to

$$w_*(\zeta_*) = \zeta_* e^{-i\alpha} + \frac{R_*^2}{\zeta_* - \mu_*} e^{i\alpha} + iK_* \log\left(\zeta_* - \mu_*\right). \tag{21}$$

The Joukowski Transform is defined by $z_*(\zeta_*)e^{i\alpha} = \zeta_* + l_*^2/\zeta_*$, where l_* is the length chosen such that the intersect in the real axis of the circle becomes the trailing edge in the transformed coordinate system. The transformed plane coordinate z_* is given by $z_* = x_* + iy_*$. The inverse transform is

$$\zeta_*(z_*) = \frac{1}{2} z_* e^{i\alpha} + \frac{z_* e^{i\alpha}}{2} \left(1 - \frac{4l_*^2}{z_*^2 e^{2i\alpha}}\right)^{1/2} \tag{22}$$

The velocity in the transformed z_* plane is given by:

$$u_*(z_*) - iv_*(z_*) = \frac{dw}{dz_*} = \frac{dw}{d\zeta_*}\frac{d\zeta_*}{dz_*} \tag{23}$$

Finally then, for a Joukowski airfoil, the potential flow velocity components are given by

$$u_{p*}(x_*, y_*) = u_{p*}(z_*) = \mathrm{Re}\left[\frac{e^{-i\alpha} - e^{i\alpha}(\zeta_*(z_*) - \mu_*)^{-2} + iK_*/(\zeta_*(z_*) - \mu_*)}{(1 - l_*^2/(\zeta_*(z_*) - \mu_*)^2)\, e^{-i\alpha}}\right], \tag{24}$$

$$v_{p*}(x_*, y_*) = v_{p*}(z_*) = -\mathrm{Im}\left[\frac{e^{-i\alpha} - e^{i\alpha}(\zeta_*(z_*) - \mu_*)^{-2} + iK_*/(\zeta_*(z_*) - \mu_*)}{(1 - l_*^2/(\zeta_*(z_*) - \mu_*)^2)\, e^{-i\alpha}}\right] \tag{25}$$

The value of K_* is chosen according to the Kutta condition to have the flow leave the trailing edge smoothly. For a symmetric airfoil this is expressed as $K_* = 2R_* \sin(\alpha)$, where R_* is the complex plane cylinder radius. We consider several cases of Joukowski airfoil: flat plate, a symmetric airfoil and cambered airfoil. In all cases the blade has chord length c and is at an angle of attack α, which selects the value of K_*. This is also the value used to reproduce the lift force in the Gaussian kernel solution derived in §3.

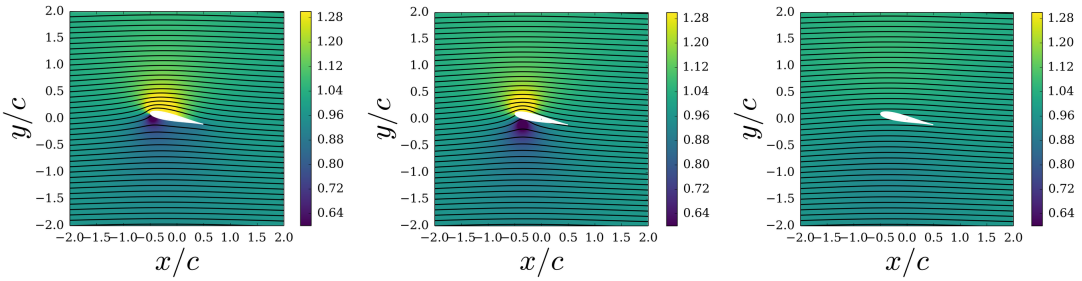

Figure 1. Contour plots of velocity magnitude and streamlines. Left: Potential flow solution for a symmetric Joukowski airfoil at $\alpha = 12^o$. Middle: Solution to linearized Euler equation with Gaussian body force with the optimal value of ϵ_*. Right: Solution to linearized Euler equation with Gaussian body force with $\epsilon_* = 1$.

Airfoil	Optimum width ϵ^{opt}/c	Optimum position s_0^{opt}/c
Flat Plate	0.17	-0.36
Symmetric	0.14 to 0.17	-0.37 to -0.35
Cambered	0.14 to 0.25	-0.37 to -0.24

Table I. Optimum width and position of Gaussian force for different airfoils.

5. MINIMIZING THE DIFFERENCE BETWEEN TWO SOLUTIONS

The solutions for flow over a Joukowski airfoil and flow over a Gaussian distributed lift force have been obtained. The latter depends upon the width parameter ϵ_* and position $\mathbf{x}_{0*}$ of the Gaussian kernel. To simplify, we assume the location of the force is located on the chord of the lifting surface and thus its position is parameterized by a single chord location $s_{0*} = s_0/c$. The dimensionless chord location s_* is defined such that $s_* = -1/2$ at the leading edge and $s_* = +1/2$ at the trailing edge. Projecting the force center position onto the Cartesian coordinate system the location of the points becomes $x_{0*} = s_{0*}\cos(\alpha)$ and $y_{0*} = -s_{0*}\sin(\alpha)$. Figure 1 shows velocity magnitude contours with streamlines for a symmetric airfoil with $\alpha = 12^o$. The potential flow solution is on the left, with the solution to the linearized Euler equation with body force using the optimum value of ϵ_* (to be determined as explained below) shown in the middle panel, and the solution with $\epsilon_* = 1$ [10] to the right. As can be seen, the velocity distribution generated by a Gaussian body force in the vicinity of the blade depends rather strongly on ϵ_*, even though the integrated quantities such as lift, momentum and very far-field perturbation velocity are, by definition, the same in all cases. This provides a motivation to establish, in a quantitative manner, the optimum value of ϵ_* and its position s_{0*}.

The optimal values of the parameters ϵ_* and s_{0*} are found by considering the following L2 norm of the difference between the two solutions:

$$E_u^2(\epsilon_*, s_{0*}) = \frac{1}{A_*}\int\int \left[(u_{\epsilon*} - u_{p*})^2 + (v_{\epsilon*} - v_{p*})^2\right] f[\zeta_*(x_*, y_*)]\, dx_* dy_* \tag{26}$$

where $f(\zeta_*)$ is a mask to establish when the solution is outside of the airfoil area (i.e. $f(\zeta_*) = 0$ when ζ_* is inside the circle in the ζ_* plane, and one otherwise), and $A_* = A/c^2$ is a fixed reference area, chosen to be the square of the chord, i.e. $A_* = 1$ (and $A = c^2$).

The error is evaluated for the flat plate and symmetric Joukowski airfoil for a number of angles of attack (and implied circulations K_*). For each case, the error is evaluated by performing the integration in equation 26 for a range of (ϵ_*, s_{0*}) values. Results are shown in Figure 2 with dashed lines showing the optimum values $(s_{0*}^{\text{opt}}, \epsilon_*^{\text{opt}})$. The error is normalized with the square error at the minimum point. The minimum at $(s_{0*}^{\text{opt}}, \epsilon_*^{\text{opt}})$ is found using the L-BFGS-B local minimizer [17, 18].

The optimal values so obtained are listed in Table I. The analysis is repeated for various angles of attack. We obtain essentially the same optimal values, independent of angle of attack α. This can be seen clearly in Figure 3 where the normalized error surface for the flat plate case is shown along the optimal values for several angles of attack. The curves show excellent collapse for different angles of attack, which indicates that the optimum values of ϵ_* and chord position s_{0*} are independent of α. While the normalized error is independent of angle of attack, the magnitude of the error depends on α. Figure 4 shows the error for a flat plate and the symmetric airfoil as function of angle of attack. The magnitude of the non-dimensional error

Wind Energ. 2015; **00**:1–14 © 2015 John Wiley & Sons, Ltd.
DOI: 10.1002/we
Prepared using weauth.cls

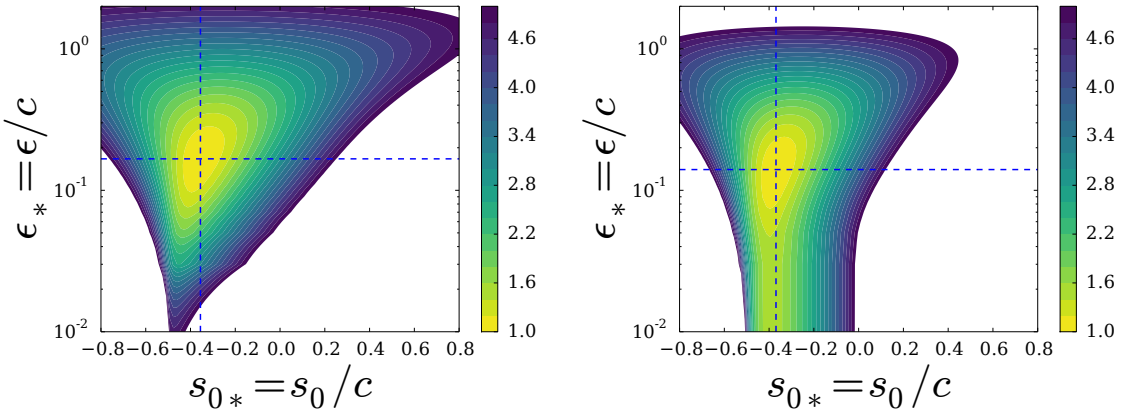

Figure 2. Square error (E_u^2/E_{u-min}^2) contours as function of force center position s_0/c and Gaussian width $\epsilon_* = \epsilon/c$ for the case with angle of attack $\alpha = 12^o$. Results are shown for a flat plate (left) and for a symmetric Joukowski airfoil (right). Vertical and horizontal lines mark the optimal value of the chord position $s_{0*}^{\rm opt}$ and $\epsilon_*^{\rm opt}$ respectively.

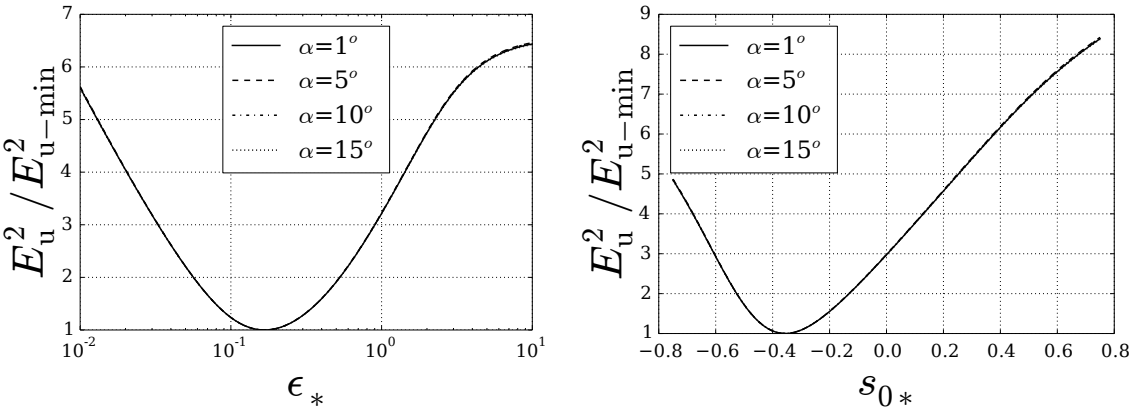

Figure 3. Normalized square error for the flat plate as a function of ϵ_* (at $s_{*0} = -0.36$) and the chord position s_{*0} (at $\epsilon_* = 0.17$ for different angles of attack.

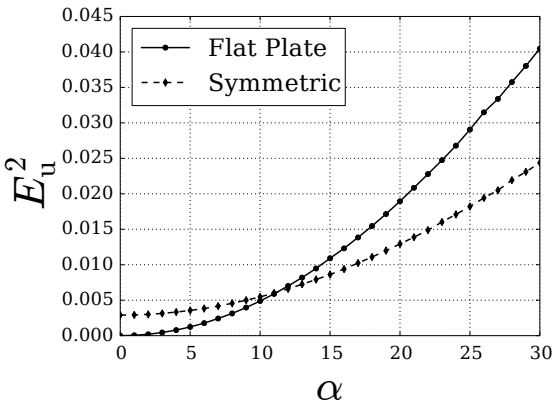

Figure 4. Squared error at the optimum values $\epsilon_*^{\rm opt}$ and chord position $s_{*0}^{\rm opt}$ as a function of angle of attack α.

for angles of attack from 0^o to 15^o ranges between 0 and 0.01 which translates to an average error of about 0 to 10% (of U_∞) in the perturbation velocity field in the relevant region.

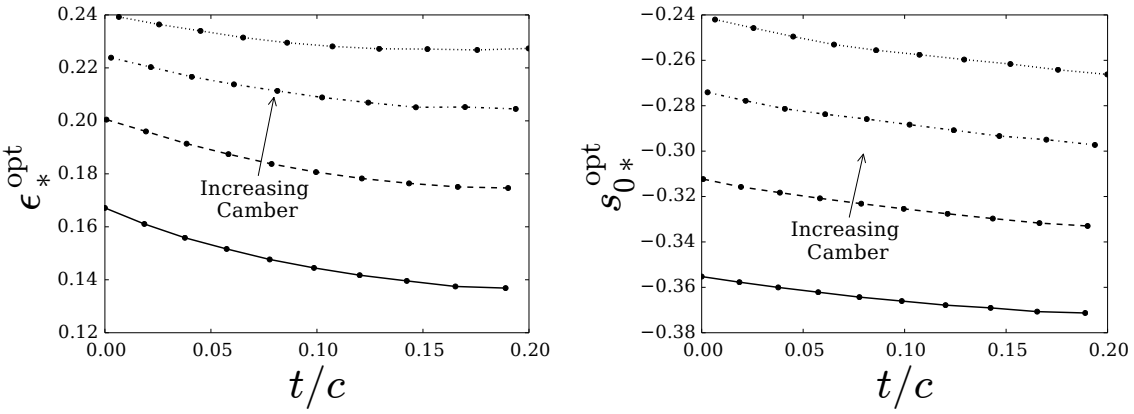

Figure 5. Optimum values $\epsilon_*^{\mathrm{opt}}$ and chord position s_{*0}^{opt} as function of thickness t/c for different camber with angle of attack $\alpha = 12^o$.

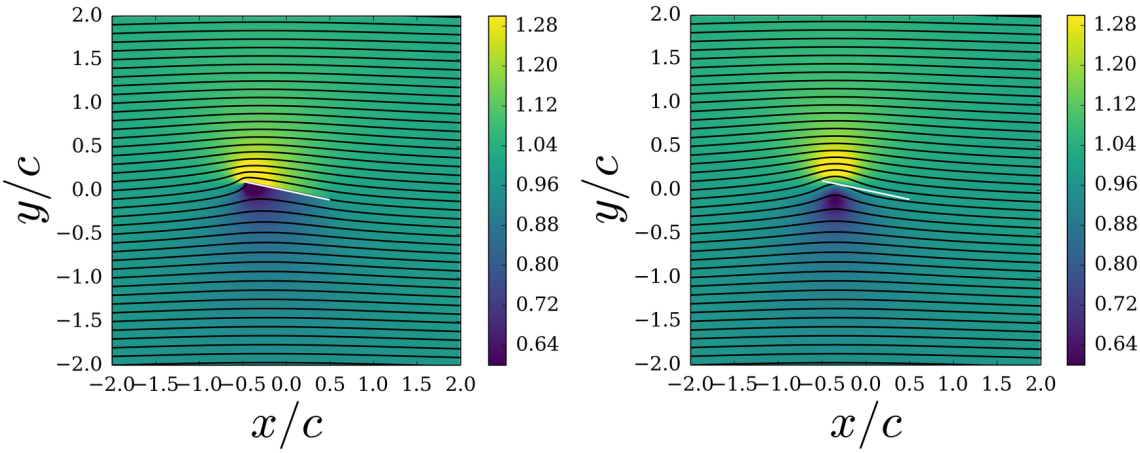

Figure 6. Visualization of potential flow solution over a Joukowski airfoil (left) and body force solution (right) for a flat plate. Colors indicate the magnitude of the velocity field while solid lines indicate streamlines.

The optimum values are a function of the thickness and camber of the airfoil. Figure 5 shows this dependency for a range of camber values and airfoil thicknesses. Camber and thickness are included by shifting the potential flow solution in the imaginary plane ζ_* by a range from $\mu/R = 0$ (flat plate) to $\mu/R = -0.1 + 0.1i$ (cambered airfoil). This range is chosen to match typical representative airfoil values [16]. The solid line in Figure 5 represents the case for a symmetric airfoil. Larger cambered airfoils require larger values of ϵ_* and the chord position of the Gaussian s_{*0}^{opt} is closer to the quarter chord. This placement allows for the streamlines to deform following the cambered airfoil surface. With more camber, the streamlines deform in a smoother way following the airfoil surface, as opposed to having a sharper deformation near the leading edge. As the airfoil becomes thicker, $\epsilon_*^{\mathrm{opt}}$ becomes smaller. The smaller $\epsilon_*^{\mathrm{opt}}$ allows the streamlines to deform more and align more closely with the airfoil surface.

Use of $\epsilon^{\mathrm{opt}}/c$ and s_0^{opt}/c gives a flow field induced by the Gaussian force field which is as close as possible to the potential flow solution. In order to visualize the two velocity fields, in Figures 6 and 7 we compare streamlines and velocity magnitudes for the Joukowski potential flow solution and the model Gaussian force induced velocity field, for the cases of a flat plate and a cambered airfoil at $\alpha = 12^o$. The case of symmetric airfoil has already been shown in Figure 1 (left and middle panels). The solutions are qualitatively similar with the main features of the flow being reproduced. Differences still exist as the streamlines in the potential flow solution are deformed when approaching the leading edge and leaving the trailing edge smoothly obeying the boundary condition at the blade surface. Conversely, in the body force solutions the streamlines can pass through the airfoil, as expected from a solution without physical boundaries on the airfoil.

Wind Energ. 2015; **00**:1–14 © 2015 John Wiley & Sons, Ltd.
DOI: 10.1002/we
Prepared using weauth.cls

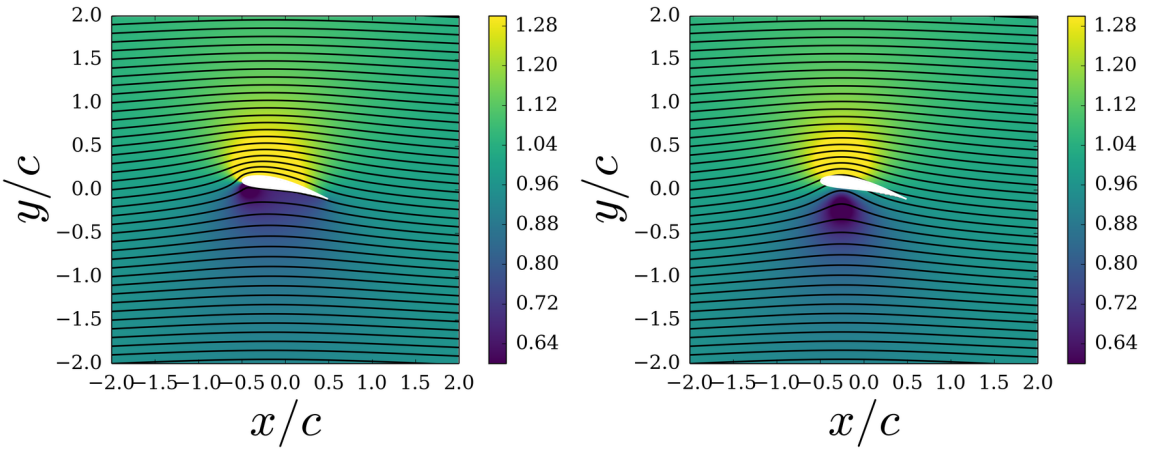

Figure 7. Same as figure 6 but for cambered airfoil case.

It is worthwhile noticing that while $\epsilon^{\text{opt}} \sim O(0.2c)$ represents a fairly small fraction of the chord, the induced velocity field, being the integral of the Gaussian vorticity distribution, has a footprint at a scale that extends to a scale on the order of c. The optimization being based on the differences among the two velocity fields emphasizes the region near the blade at distances on the order of c. It is also noted that in the far field both solutions agree exactly with the ideal vortex tangential velocity distribution that decays as $\Gamma/(2\pi r)$, because by construction both the Gaussian forced velocity and the potential flow solution share the same imposed circulation and free-stream velocity.

5.1. Optimal drag kernel width

Returning now to the issue of representing drag forces, the y-direction far-field Gaussian wake shape in Eq. 15 suggests that in ALM, the drag force can be implemented using a kernel width ϵ_{d*} that can differ from that used for the lift force. Specifically, it can be chosen so as to mimic the initial width of the wake. At $x_* >> 1$, the velocity defect integrates to $c\, U_\infty c_d/2$ as required by deficit momentum flux conservation. Thus choosing $\epsilon_d = c\, c_d/2$, i.e. the momentum thickness, should give realistic initial wake distributions. We remark that this choice implies that the nonlinearity parameter is $u'/U_\infty = 1/2\sqrt{\pi} \approx 0.28$, and so it is possible that nonlinear effects begin to distort the velocity profile downstream when using such a kernel, but anyhow downstream mixing and growth of the wake will naturally be accounted for by turbulence resolving or modeling parts of the LES.

We remark that for instance highly stalled blades could be represented with larger ϵ_{d*} than cases with initially very thin wakes. In time-dependent stall situations (e.g. in ALM simulations of vertical axis wind turbines), one may allow the kernel width to change in time. Figure 8 shows the vorticity distribution for a drag force with ϵ_d chosen to be equal to the momentum thickness.

6. GENERALIZATION: 2D GAUSSIAN KERNEL

The geometry of a typical airfoil is elongated in the x-axis and much thinner in the y-axis. For this reason we now generalize the formulation presented for a circular Gaussian kernel to an elliptical Gaussian kernel with different widths in the x- and y-directions. For simplicity we first consider the semi-axes aligned with x-y coordinate system:

$$\eta_\epsilon = \frac{1}{\epsilon_x \epsilon_y \pi^2} e^{-\left(x^2/\epsilon_x^2 + y^2/\epsilon_y^2\right)}. \tag{27}$$

The idea is to optimize the values of both ϵ_x and ϵ_y by, again, minimizing the error defined in equation 26. We seek a solution to the problem in a similar way to Section 3. After the linearization of the equations we obtain an expression for the vorticity perturbation

$$\omega'_{\epsilon*}(x_*, y_*) = -\frac{2K_*}{\epsilon_{x*}\epsilon_{y*}} e^{-(x_*^2/\epsilon_{x*}^2 + y_*^2/\epsilon_{y*}^2)}. \tag{28}$$

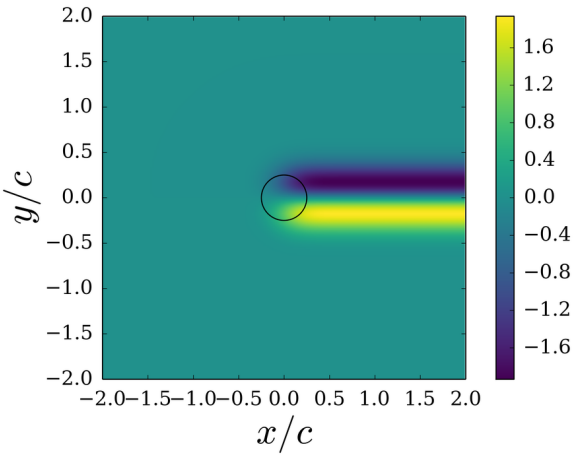

Figure 8. Vorticity perturbation distribution ω'_* for a case with $\epsilon_{d*} = c_d/2$. The circle represents the value of ϵ_{d*}.

The equation can be written in terms of the streamfunction as the Poisson equation

$$\nabla^2\psi' = -\omega'_{\epsilon*}(x_*, y_*) = \frac{2K_*}{\epsilon_{x*}\epsilon_{y*}} e^{-(x_*^2/\epsilon_{x*}^2 + y_*^2/\epsilon_{y*}^2)}. \tag{29}$$

The equation can be written in Fourier space

$$\widetilde{\psi'}(k_x, k_y) = -\frac{\widetilde{\omega'_{\epsilon*}}(k_x, k_y)}{k_x^2 + k_y^2} = -\frac{K_* e^{-(k_x^2\epsilon_{x*}^2 + k_y^2\epsilon_{y*}^2)/4}}{k_x^2 + k_y^2}. \tag{30}$$

The kernel can be rotated in space according to the angle of attack by a simple transformation with $x' = x\cos\alpha - y\cos\alpha$ and $y' = x\sin\alpha + y\sin\alpha$. The same transformation is done to the wave numbers k_x and k_y in Fourier Space in order to rotate the solution by the given angle of attack α. Eq. 30 is solved by using the Fast Fourier Transform algorithm [19] as implemented in the numpy library [18]. The solution is periodic, so artificial counter rotating vortices are created near the edges to artificially recover periodicity in the solution. In order to overcome this, a solution for the problem in Fourier Space (Eqs. 30 with $\epsilon_{*y} = \epsilon_{*x}$) is subtracted from the solution (Eq. 30). The solution to the problem with $\epsilon_{*y} = \epsilon_{*x}$ (Eqs. 10—11) is then added back in real space to obtain the final form of the solution. This method eliminates the opposing artificial circulation from the edges, where the true solution must behave as an ideal vortex far away from the center for both cases ($\epsilon_x = \epsilon_y$ and $\epsilon_x \neq \epsilon_y$).

The same optimization algorithm as in Section 5 is used to find the optimum values for the kernel widths ϵ_{x*}, ϵ_{y*} and the position s_{0*}. Figure 9 shows contours of the normalized square error as a function of ϵ_{x*} and ϵ_{y*}. It is seen that the optimum value is much more sensitive to the width in the direction of the chord ϵ_{x*} than in the direction of thickness ϵ_{y*}. This method provides solutions with smaller errors than the cases with $\epsilon_{x*} = \epsilon_{y*}$ shown in Section 5. The dashed diagonal line in Figure 9 shows the case of $\epsilon_{x*} = \epsilon_{y*}$, which lies above the optimal values for the elliptical case. This line shows that even though the optimal values for the case with $\epsilon_{x*} \neq \epsilon_{y*}$ improve the error as compared to the circular Gaussian, the error is still within the same order of magnitude. The difference in error magnitude is shown in Figure 10, where the error is improved by more than 50% for cases of a flat plate and symmetric airfoil for higher angles of attack.

The optimum values are independent of angle of attack as shown in Figure 11. The error is more sensitive to variation in ϵ_{*x}, after ϵ_{y*} reaches a value on the order of $\epsilon_{y*} \sim 10^{-2}$, the error reaches a threshold and smaller values do not provide improved results. This solution is similar to an actuator surface method, but with a vorticity distribution along the chord given by the Gaussian field with an optimal ϵ_{x*}. In this case, the center location of the surface is near the quarter chord as shown previously in Section 5. The kernel widths ϵ_{x*} and ϵ_{y*} are always smaller than the chord. Figure 12 shows the distribution of $\epsilon_{x*}^{\text{opt}}$ and chord position s_0^{opt} for different thicknesses and camber. The values for $\epsilon_{x*}^{\text{opt}}$ are larger than for the 1D case. The optimal location s_0^{opt} is very similar to the 1D case.

Figures 13 and 14 show velocity contours for the cases with optimal ϵ_{x*} and ϵ_{y*}. The most noticeable feature of the velocity field induced by the elliptical 2D Gaussian lift force kernel is that the deformation of the streamlines agrees better with the potential flow solution than the circular Gaussian kernel case considered in Section 3.

Wind Energ. 2015; **00**:1–14 © 2015 John Wiley & Sons, Ltd.
DOI: 10.1002/we
Prepared using weauth.cls

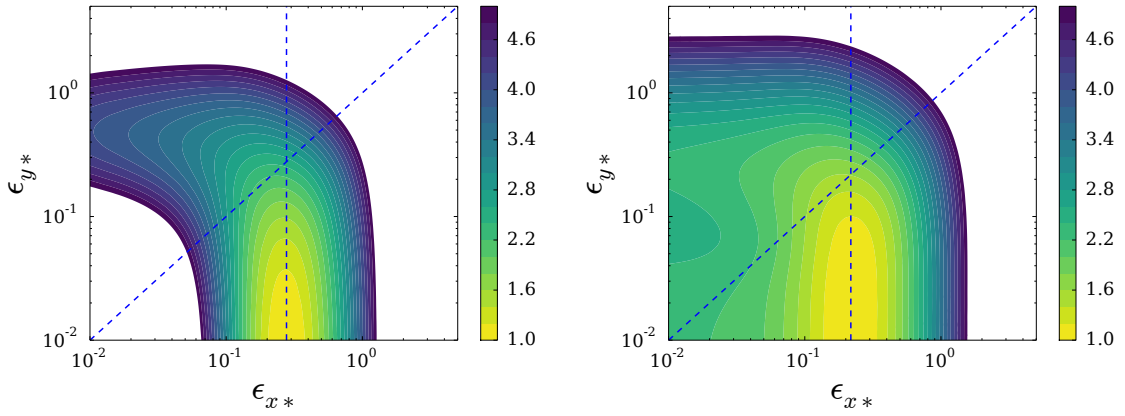

Figure 9. Normalized square error (E_u^2/E_{u-min}^2) contours as function of Gaussian width ϵ_{x*} and ϵ_{y*} for the case with angle of attack $\alpha = 12^o$. Results are shown for a flat plate (left) and for a symmetric Joukowski airfoil (right). Vertical lines mark the optimal value of ϵ_{x*}, while the optimal value for ϵ_{y*} tends to zero. The diagonal line marks the case with $\epsilon_{x*} = \epsilon_{y*}$.

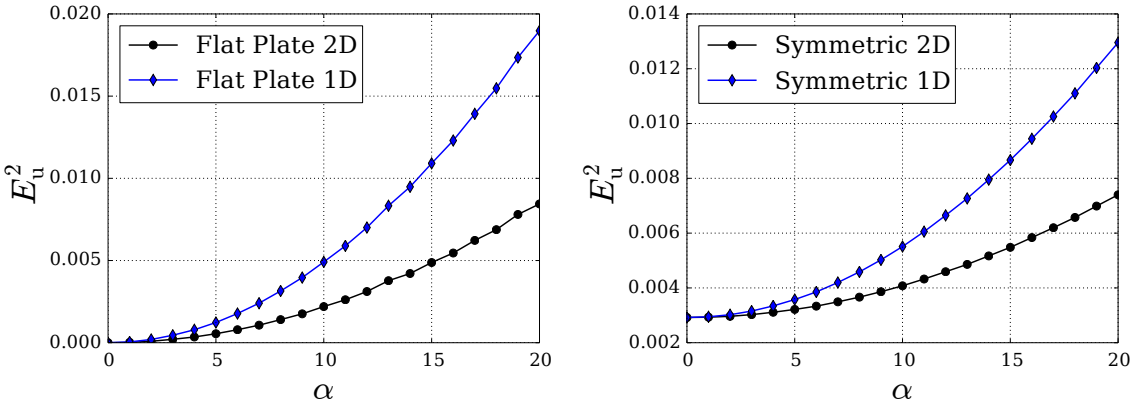

Figure 10. Squared error at the optimum values $\epsilon_{x*}^{\text{opt}}$, $\epsilon_{y*}^{\text{opt}}$ and chord position s_{*0}^{opt} as a function of angle of attack α for a flat plate (left) and Symmetric airfoil (right).

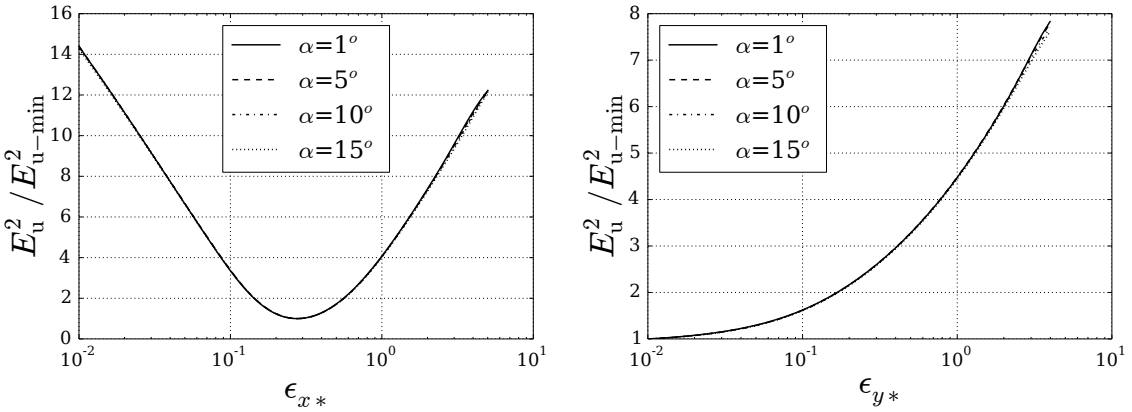

Figure 11. Normalized squared error as a function of ϵ_x (left) and ϵ_y (right) for a flat plate at different angles of attack.

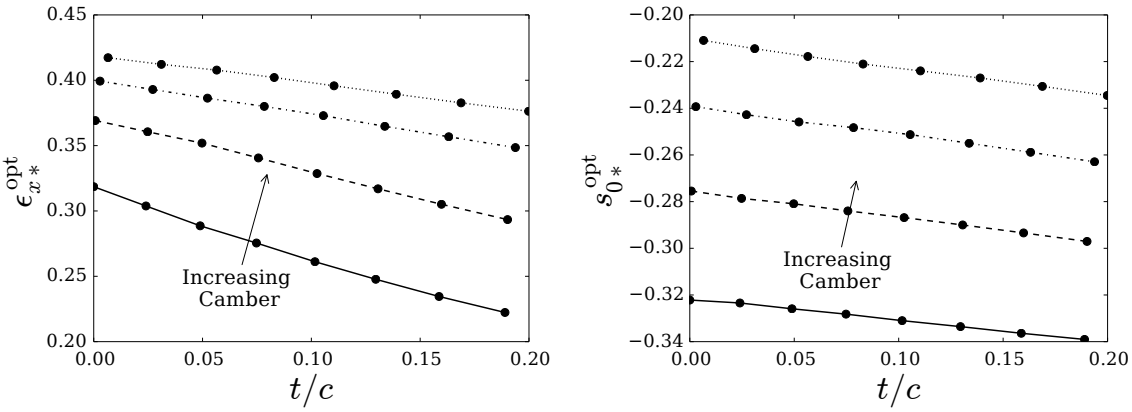

Figure 12. Optimum values $\epsilon^{\rm opt}_{x*}$ and chord position $s^{\rm opt}_{*0}$ as function of thickness t/c for different camber with angle of attack $\alpha = 12^o$.

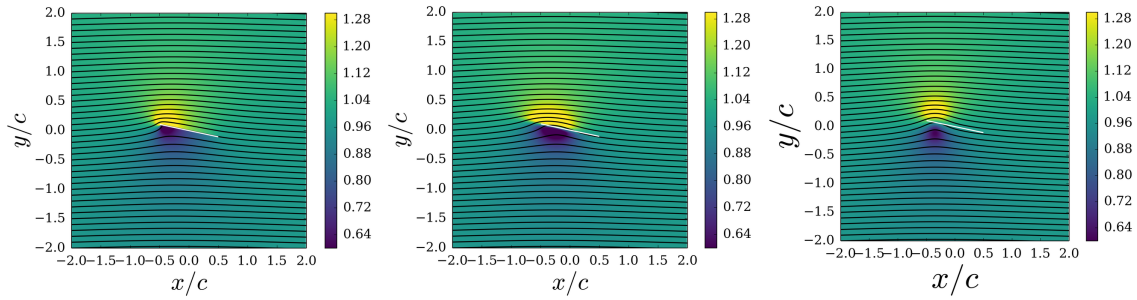

Figure 13. Visualization of potential flow solution over a Joukowski airfoil (left), body force solution with ϵ_{x*} and ϵ_{y*} (middle) and body force solution with 1D Gaussian (right) for a flat plate. Colors indicate the magnitude of the velocity field while solid lines indicate streamlines.

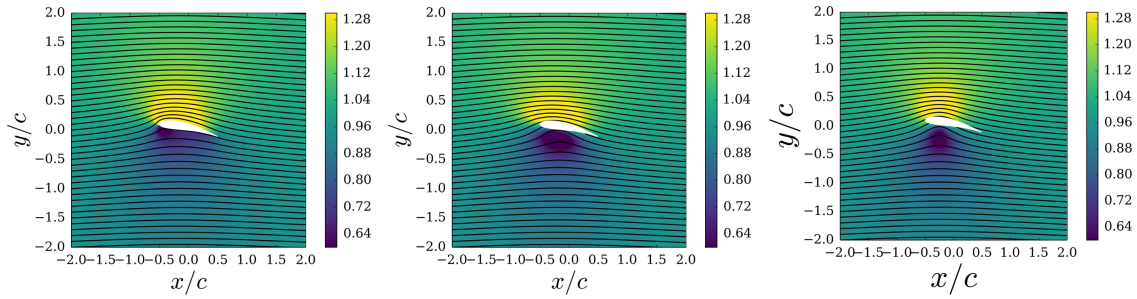

Figure 14. Same as Figure 13 but for cambered airfoil case.

7. CONCLUSIONS

By examining the velocity field induced by a circular Gaussian body force and comparing it with the velocity field one wishes to approximate (e.g. flow over an airfoil with uniform inflow), we can provide a criterion to select an optimum value of the force width ϵ and its position along the chord s_0. The analytical solution for the velocity field induced by a Gaussian body force is obtained using a perturbation analysis, i.e. for a linearized advection velocity. Thus the analytical solution obtained is expected to become less accurate for large applied forces that cause significant velocity perturbations compared to U_∞.

We applied the method for both lift and drag forces. First, the solutions were used to show that the common method of sampling the velocity at the center of the Gaussian provides the correct reference velocity due to the symmetric vorticity distribution that results from applying a Gausian lift force. For the case of drag, a reference velocity correction factor was developed which depends on the ratio of the momentum thickness and kernel width used to specify the drag force.

Wind Energ. 2015; **00**:1–14 © 2015 John Wiley & Sons, Ltd.
DOI: 10.1002/we
Prepared using weauth.cls

Then solutions were used to determine the optimal kernel width ϵ. In the case of a flat plate, to represent lift the values $\epsilon/c = 0.17$ and $s_0/c = -0.36$ provide the optimum. For the case of a symmetric Joukowski airfoil the values are within a range of $\epsilon/c = 0.14$ to 0.17 and $s_0/c = -0.37$ to -0.35, essentially the same as those for the flat plate. We also found that these values do not depend strongly on angle of attack. Further similar calculations for cambered airfoil provided very similar results but with a wider range of values from $\epsilon/c = 0.14$ to 0.24 and $s_0/c = -0.37$ to -0.24 depending on camber and thickness.

The results from the theoretical analysis have the following practical implications: When using ALM with LES grid resolutions at or larger than the chord-length, the choice of ALM smoothing kernel scale must be dictated by LES numerical considerations, as is often done in practice [4, 10, 11]. Conversely, if the LES grid resolution is sufficiently refined to place a number of grid points along the chord of the lifting surface, then best results should be obtained when using a "lift force" Gaussian kernel with the physically optimal width and location determined in the present calculations. The results presented are only for Joukowski airfoils, nevertheless, given the relative insensitivity of ϵ_{opt}/c, for example, the flat plate and cambered airfoil cases we expect the obtained $\epsilon_{\text{opt}}/c \sim 0.2$ value to be approximately valid for other types of airfoils. Values close to the optimal should provide smaller errors when trying to replicate the flow field of a 2D airfoil. A 2D elliptical Gaussian kernel with a width ϵ_{x*} in the direction of the chord and ϵ_{y*} in the thickness direction can provide even more accurate results than a circular Gaussian kernel. The velocity error for this kernel is further reduced compared to the 1D kernel. The position of this 2D kernel in the chord is similar to the 1D kernel s_0/c. For the drag force, a separate Gaussian force with kernel width that scales with the wake momentum thickness could be used to generate a velocity wake profile with a realistic initial thickness. The results shown are for 2D lift and drag forces. Future work includes testing these optimal values in the case of a 3D rotor, with special interest in the tips of a rotating blade.

ACKNOWLEDGEMENTS

The authors thank Xiang I.A. Yang, Perry Johnson and Philippe Spalart for a number of important ideas and suggestions at various stages of this work. The research was supported by the National Science Foundation grants no. IGERT 0801471, 1243482 (the WINDINSPIRE project) and 1230788. Numerical implementation and plots were generated using python with scipy, numpy and matplotlib libraries.

REFERENCES

[1] J. N. Sørensen. Aerodynamic Aspects of Wind Energy Conversion. *Annual Review of Fluid Mechanics*, 43(1):427–448, January 2011.

[2] A. Jimenez, A. Crespo, E. Migoya, and J. Garcia. Advances in large-eddy simulation of a wind turbine wake. *Journal of Physics: Conference Series*, 75:012041, July 2007.

[3] M. Calaf, C. Meneveau, and J. Meyers. Large eddy simulation study of fully developed wind-turbine array boundary layers. *Physics of Fluids*, 22(1):015110, 2010.

[4] J. N. Sørensen and W. Z. Shen. Numerical Modeling of Wind Turbine Wakes. *Journal of Fluids Engineering*, 124(2):393–399, June 2002.

[5] R. Mikkelsen, J. N. Sørensen, S. Øye, and N. Troldborg. Analysis of power enhancement for a row of wind turbines using the actuator line technique. In *Journal of Physics: Conference Series*, volume 75, page 012044, 2007.

[6] N. Troldborg, J. N. Sørensen, and R. Mikkelsen. Numerical simulations of wake characteristics of a wind turbine in uniform inflow. *Wind Energy*, 13(1):86–99, 2010.

[7] F. Porté-Agel, Y. T. Wu, H. Lu, and R. J. Conzemius. Large-eddy simulation of atmospheric boundary layer flow through wind turbines and wind farms. *Journal of Wind Engineering and Industrial Aerodynamics*, 99(4):154–168, 2011.

[8] M. J. Churchfield, S. Lee, J. Michalakes, and P. J. Moriarty. A numerical study of the effects of atmospheric and wake turbulence on wind turbine dynamics. *Journal of Turbulence*, 13:N14, January 2012.

[9] M. J. Churchfield, S. Lee, P. J. Moriarty, L. A. Martínez, S. Leonardi, G. Vijayakumar, and J. G. Brasseur. A large-eddy simulation of wind-plant aerodynamics. *AIAA paper*, (2012-0537), 2012.

[10] L. A. Martínez-Tossas, M. J. Churchfield, and S. Leonardi. Large eddy simulations of the flow past wind turbines: actuator line and disk modeling. *Wind Energy*, 18(6):1047–1060, 2015.

[11] Pankaj K Jha, Matthew J Churchfield, Patrick J Moriarty, and Sven Schmitz. Guidelines for volume force distributions within actuator line modeling of wind turbines on large-eddy simulation-type grids. *Journal of Solar Energy Engineering*, 136(3):031003, 2014.

[12] S. Xie and C. Archer. Self-similarity and turbulence characteristics of wind turbine wakes via large-eddy simulation: Self-similarity and turbulence of wind turbine wakes via LES. *Wind Energy*, 18(10):1815–1838, October 2015.

[13] Wen Zhong Shen, Jian Hui Zhang, and Jens Nørkær Sørensen. The actuator surface model: a new navier–stokes based model for rotor computations. *Journal of Solar Energy Engineering*, 131(1):011002, 2009.

[14] C. Sibuet Watters, S.P. Breton, and C. Masson. Application of the actuator surface concept to wind turbine rotor aerodynamics. *Wind Energy*, 13(5):433–447, 2010.

[15] J. R. Forsythe, E. Lynch, S. Polsky, and P. Spalart. Coupled Flight Simulator and CFD Calculations of Ship Airwake using Kestrel. *AIAA paper*, January 2015.

[16] J. Katz and A. Plotkin. *Low-Speed Aerodynamics*. Cambridge University Press, February 2001.

[17] R. Byrd, P. Lu, J. Nocedal, and C. Zhu. A Limited Memory Algorithm for Bound Constrained Optimization. *SIAM Journal on Scientific Computing*, 16(5):1190–1208, September 1995.

[18] T. E. Oliphant. Python for Scientific Computing. *Computing in Science Engineering*, 9(3):10–20, May 2007.

[19] James W Cooley and John W Tukey. An algorithm for the machine calculation of complex fourier series. *Mathematics of computation*, 19(90):297–301, 1965.

Wind Energ. 2015; **00**:1–14 © 2015 John Wiley & Sons, Ltd.
DOI: 10.1002/we
Prepared using weauth.cls